



Ultra-Range Bimetallic Pt–Pd Nanospheres Deposited on Reduced Graphene Sheet as Efficient Electrocatalyst Towards Electrooxidation of Methanol

G. Sreenivasa Kumar¹ · N. Ramamanohar Reddy¹ · B. Sravani² · L. Subramanyam Sarma² · T. Veera Reddy³ · V. Madhavi⁴ · S. Adinarayana Reddy¹

Received: 20 September 2019 / Published online: 20 December 2019
© Springer Science+Business Media, LLC, part of Springer Nature 2019

Abstract

Direct methanol fuel cells (DMFCs) offers promising possibilities in meeting future energy needs in a most sustainable way. To electro oxidize methanol at anode of DMFCs, till date Pt and Pt-based materials were widely employed. To improve the utilization of precious metals it is highly desirable to disperse them on conductive carbon structures. Here, we synthesized ultra-range bimetallic platinum–palladium (Pt–Pd) nanospheres (NSs) with uniform dispersion on reduced graphene oxide (RGO) sheets by a simple hydrothermal method and studied their efficacies towards methanol oxidation reaction (MOR). From HR-TEM analysis, it was found that the synthesized bimetallic Pt–Pd NSs possess an average particles size of about 5 to 7 nm consistent with XRD data. The MOR electro catalytic activity of bimetallic PtPd-RGO NSs was higher compared to homemade mono metallic Pt-RGO, Pd-RGO catalysts and commercial E-tekPt/C.

Keywords Ultra-range bimetallic Pt–Pd NSs · RGO sheets · Electrocatalysis · Energy conversion

Introduction

Rapidly increasing energy demands and environmental concerns prompted researchers to find ways to replace traditional fossil fuels and to focus more on exploring efficient clean energy sources with either completely carbon-free emissions or extremely low carbon emissions [1]. With many attributes like high power density, high energy-conversion efficiency, and low pollution concerns, fuel cells either methanol-fed or hydrogen-fed are emerging as most promising energy conversion systems [2–5].

However, to realize the commercial viability of fuel cells it is very important to develop electrocatalysts with high efficacies towards anodic methanol oxidation reaction and cathodic oxygen reduction reactions [6–11]. Considering the development of electrocatalysts, both the electrocatalytic activity and durability of catalysts are both indispensable for the practical application of DMFCs. Therefore, it is expected that judicious balance between catalytic activity and durability may provide solutions to realize the improved kinetic rate of either MOR or ORR or both. Platinum has been widely applied as an MOR electrocatalyst in DMFCs owing to its unique electrocatalytic properties [12–17]. To improve the CO-tolerance as well as to reduce the loading of platinum, many efforts are directed to develop platinum-based bimetallic nanoparticles such as PtAu, PtAg, PtRu, PtPd and PtNi and in many cases alloyed configurations exhibited enhanced electro catalytic activity [18–28]. Among these materials, the PtPd bimetallic nanoparticles express excellent electrocatalytic performance along with long-term stabilities than the other Pt-based bimetallic catalysts [29–32]. Recently, graphene and its derivatives such as graphene oxide (GO) has attracted intense fundamental and applied research interest

✉ S. Adinarayana Reddy
anreddyphd@gmail.com

¹ Department of Materials Science and Nanotechnology, Yogi Vemana University, Kadapa, AP 516 005, India

² Department of Chemistry, Yogi Vemana University, Kadapa, A.P. 516 005, India

³ Department of Chemistry, Vikrama Simhapuri University, Nellore, A.P. 524320, India

⁴ Department of Instrumentation and Applied Physics, Indian Institute of Science, Bangalore, India

due to its outstanding properties such as good electronic conductivity, high theoretical surface area ($2600 \text{ m}^2/\text{g}$), high durability, mechanical, thermal stability and widely used as a support material for the catalyst in fuel cell applications [33, 34]. Even, good number of recent research has demonstrated the loading of bimetallic alloy catalysts on a conductive carbonaceous supporting substrates, such as graphene nanosheets (GNS), carbon nanotubes, and carbon nanoribbons etc. [35–38].

Motivated by these studies, we fabricated the ultra-range bimetallic Pt–Pd nanospheres deposited on reduced graphene sheet towards electrooxidation of methanol by a hydrothermal method and labeled the catalyst as Pt–Pd/RGO NSs. The fabricated Pt–Pd/RGO NSs were thoroughly characterized for structure, morphology, particle size distribution of electrocatalyst and nature of functional groups on reduced graphene oxide using X-ray diffraction, FT-IR, Raman, SEM, TEM including HRTEM, EDX. Further, electrocatalytic activities and stabilities of the prepared bimetallic Pt–Pd/RGO NSs, monometallic Pt/RGO, Pd/RGO and commercial E-tekPt/C are evaluated in 1 M methanol + 0.5 M H_2SO_4 solutions using cyclic voltammetry (CV) and chrono amperometry (CA). When compared to the monometallic Pt/RGO, Pd/RGO, commercial E-tekPt/C, the synthesized Pt–Pd/RGO NSs exhibited enhanced methanol oxidation activity.

Experimental

Materials

Graphite powder, Na_2PdCl_4 , $\text{H}_2\text{PtCl}_6 \cdot 6\text{H}_2\text{O}$, NaBH_4 , and Nafion solutions were purchased from sigma Aldrich Corporation, India. KMnO_4 , H_2SO_4 , NaNO_3 , H_2O_2 , HCl , NaOH , and CH_3OH were purchased from Merck's laboratory Private limited, India.

Preparation of Graphene Oxide

Graphene oxide was prepared by a modified Hummer's method [25]. In a typical synthesis, 5 g of pure graphite powder was first dispersed in 115 mL of concentrated sulphuric acid in a 1000 mL beaker under ice bath with magnetic stirring and 15 g of potassium permanganate (KMnO_4) was slowly introduced into the mixture under ice bath with continuous stirring for 30 min followed by the addition of 2.5 g of sodium nitrate and kept it for 1 h. Later, the beaker was removed from the ice bath and stirred at room temperature for 1 h. The reaction mixture was heated on a water bath at 35°C for 30 min under continuous stirring. To this, 800 mL of double distilled water was added and raised the temperature slowly up to 98°C for 15 min under vigorous magnetic stirring and then cooled to room temperature. Finally, 30 mL of hydrogen peroxide (H_2O_2) was added to remove the excess KMnO_4 residues.

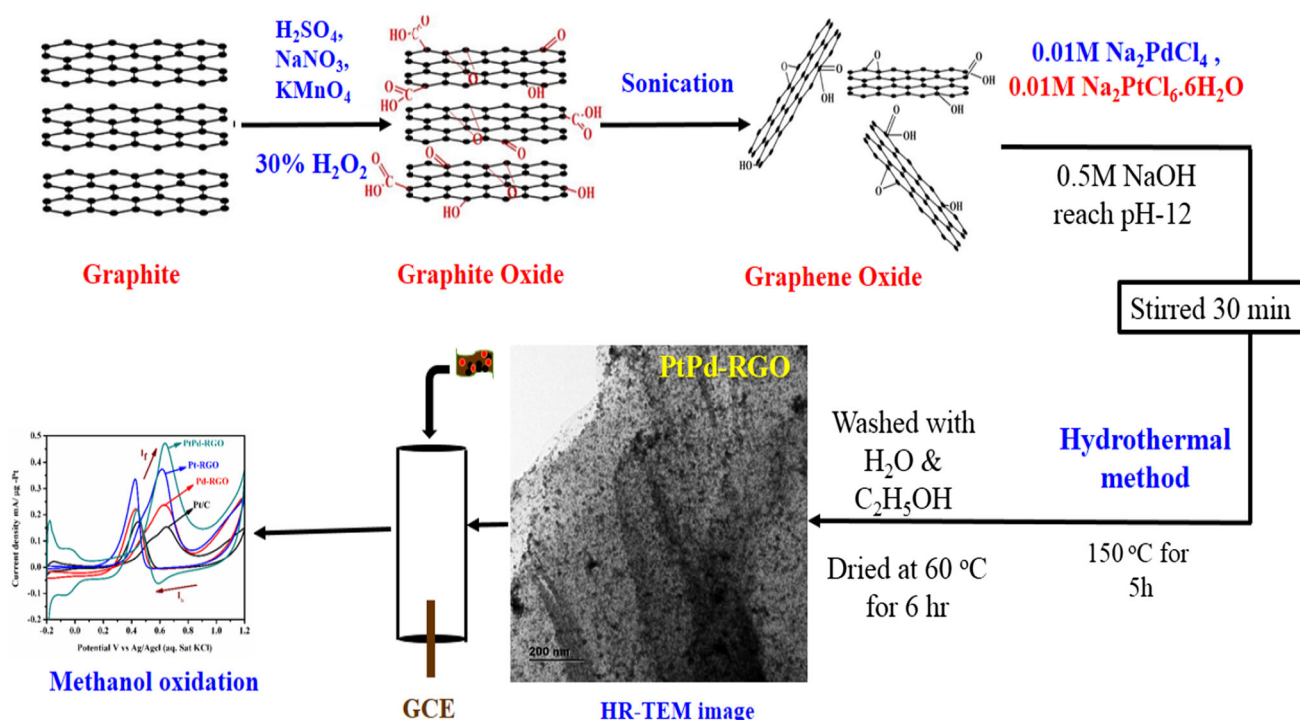


Fig. 1 Preparation of PtPd-RGO catalyst by hydrothermal method

It was washed with 1 M of hydrochloric acid (HCl) and first followed by washing with double distilled water until pH reaches to 7 and finally centrifuged. The resulting compound was dried at 60 °C in a vacuum oven for 8 h.

Preparation of PtPd-RGO NSs Electrocatalysts

Ultra-range bimetallic PtPd- nanospheres were deposited on reduced graphene sheets by a hydrothermal method. Briefly, 20 mg of graphene oxide (GO) was dispersed in 20 mL of distilled water in a round-bottomed flask under ultrasonic treatment for 1 h. Later, 25 mL of 0.01 M Na_2PdCl_4 solution (50 wt%) and 25 mL of 0.01 M of $\text{H}_2\text{PtCl}_6 \cdot 6\text{H}_2\text{O}$ solution (30 wt%) were added to GO dispersion under ultrasonication for 30 min followed by slow addition of 0.5 mL of NaOH solution until pH reaches to 12 and continued the ultrasonication for further 1 h. To this, 40 mg of NaBH_4 was added to the reaction mixture until the reaction mixture colour was changed from light brown to black under ultrasonication for 30 min. Later, the above solution was transferred into a Teflon-lined stainless steel autoclave and kept in a hot air oven at 150 °C for 5 h. Finally, the obtained PtPd-RGO NSs powders were washed with double distilled water followed by ethanol and centrifuged. The resulting compound was dried at 60 °C in a vacuum oven for 6 h. For comparison, similar procedure was adopted for the synthesis of Pt-RGO and Pd-RGO catalyst. A schematic representation of fabrication procedure adapted for Pt–Pd/RGO NSs is shown in Fig. 1.

Characterization

Electrocatalysts prepared in this study were characterized by using diffraction and microscopy techniques. XRD measurements were performed on a Miniflex 600 Rigaku X-ray diffractometer using a $\text{Cu K}\alpha$ radiation of 1.5406 Å. Raman spectra was recorded using a WiTec alpha 200 SNOM Raman spectrometer, Germany. Fourier transformed infrared spectroscopy (FT-IR) measurements of catalysts powders were performed on a Perkin Elmer Spectrum Two™ FT-IR spectrometer. Surface morphology of the obtained materials was studied by a Scanning Electron Microscope (JEOL JSM-IT500). Catalyst size, shape and chemical composition was analyzed by using High Resolution-Transmission Electron Microscopy (HR-TEM) along with Energy Dispersive Spectroscopy (EDS) (JEOL JEM 2100) at an accelerating voltage of 200 keV. X-ray photoelectron spectroscopy (XPS) measurements on Pt–Pd/RGO sample was performed with a KRATOS AXIS 165 (Canada) photoelectron spectrometer operated with a $\text{Mg K}\alpha$ radiation.

Electrochemical measurements were done by using CHI potentiostat (Model CHI 6002 E, USA) using a

conventional three-electrode electrochemical cell consisting of a Pt wire electrode, a saturated Ag/AgCl (satd. KCl) electrode, catalyst-coated glassy carbon disk (GCE, geometric area of 0.0706 cm^2) as counter, reference, and working electrodes, respectively. For the preparation of working electrode, the GCE was polished carefully with 0.05, 0.5 and 1 μm of alumina powder, and washed with ethanol and distilled water for 3 times and finally exposed to ultrasonication in. Later, 2 mg of finely grinded catalyst powder was dispersed in a mixture of ethanol (700 μL), distilled water (800 μL) and 0.5 wt% Nafion solution (100 μL) followed by ultrasonication for 1 h to form homogeneous catalyst slurry. A 5 μL of catalyst slurry was carefully deposited on a GCE surface by micropipette and dried at room temperature for overnight before carrying out the electrochemical measurements.

The CV measurements were performed in N_2 -saturated freshly prepared 0.5 M H_2SO_4 electrolyte solution by potential window between -0.2 to 1.2 V vs. Ag/AgCl (saturated KCl) at a scan rate 50 mV s^{-1} . The methanol oxidation reaction performance was investigated by performing CV measurements in a mixture of 0.5 M H_2SO_4 + 1 M CH_3OH solution with same potential window and

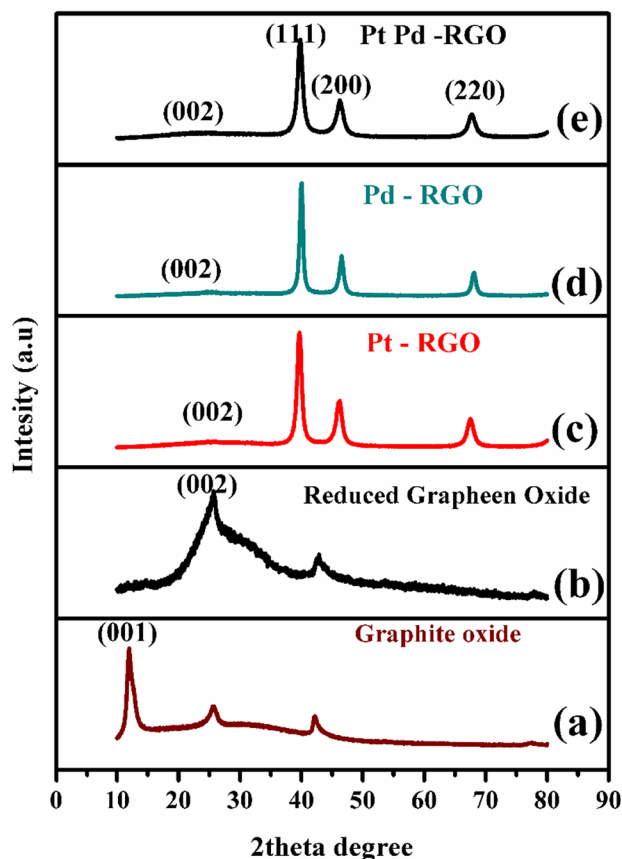


Fig. 2 XRD of a GO, b reduced graphene oxide (RGO), c Pt-RGO, d Pd-RGO and e PtPd-RGO

scan rate. Chronoamperometric measurements were done in 0.5 M H₂SO₄ + 1 M CH₃OH solution at a fixed potential of 0.62 V vs. Ag/AgCl (saturated KCl).

Results and Discussion

The crystalline nature and orientation of GO, RGO, Pt-RGO, Pd-RGO and PtPd-RGO ultra range bimetallic nanospheres was analyzed by powder X-ray diffraction (PXRD) as shown in Fig. 2. The XRD peak of GO located at 11.5° corresponding to (001) plane due to the presence of oxygen-containing functional groups introduced during exfoliation of graphite sheets. In case of RGO peak located at 25.6° corresponding to (002) diffraction plane of carbon indicative of reduction of GO to RGO. For the PtPd-RGO ultra range bimetallic nanospheres, strong diffraction peaks appeared at 39.85°, 46.19° and 67.70° could be conveniently assigned to the diffraction from (111), (200) and (220) planes, respectively. From Fig. 2c and d, Pt/RGO and Pd/RGO display peaks corresponding to those of fcc Pt (JCPDF 04-0802) and Pd (JCPDF46-1043), respectively. The average crystallite size (*D*) of the synthesized

compounds was calculated using the Debye–Scherer equation (Eq. 1).

$$D = \frac{0.9\lambda}{\beta \cos \theta} \quad (1)$$

where λ , β , θ are the wavelength of X-ray radiation used (CuK α = 0.154056 nm), the full-width-at-half maximum (FWHM) of diffraction peak and the Bragg diffraction angle, respectively. The average crystallite size (*D*) determined as 9, 12 and 7 nm for Pt-RGO, Pd-RGO and PtPd-RGO, respectively. For the sample, PtPd/RGO NSs particle size was calculated from HR-TEM image by image J software and found to be 5 to 7 nm consistent with XRD results.

Raman spectroscopy is a powerful and nondestructive tool to differentiate ordered and disordered crystal structures of carbon materials. Figure 3 shows the Raman spectra of GO, RGO, Pt-RGO, Pd-RGO and PtPd-RGO samples. The spectra shows two broad bands centered at 1349 and 1584 cm⁻¹, which correspond to low order states of the sp³ (D-band) and sp² (G-band) configurations of the carbon atoms, respectively, indicative of the existence of graphene in the catalysts. The ratio of the intensities of the D (I_D) and G (I_G) bands, I_D/I_G, used to be a measure of the

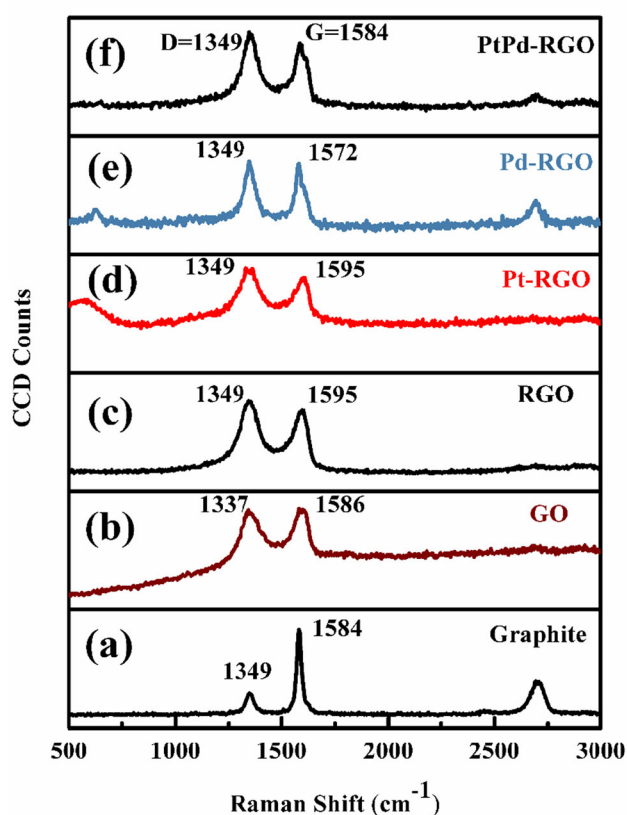


Fig. 3 Raman Spectra of a graphite, b GO, c RGO, d Pt-RGO, e Pd-RGO and f PtPd-RGO

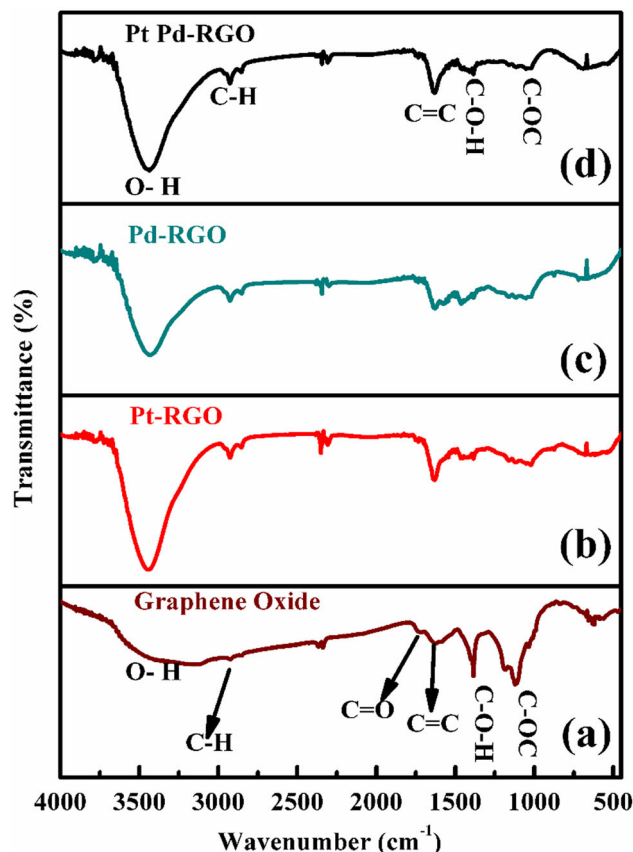


Fig. 4 FTIR of a GO, b Pt-RGO, c Pd-RGO and d PtPd-RGO

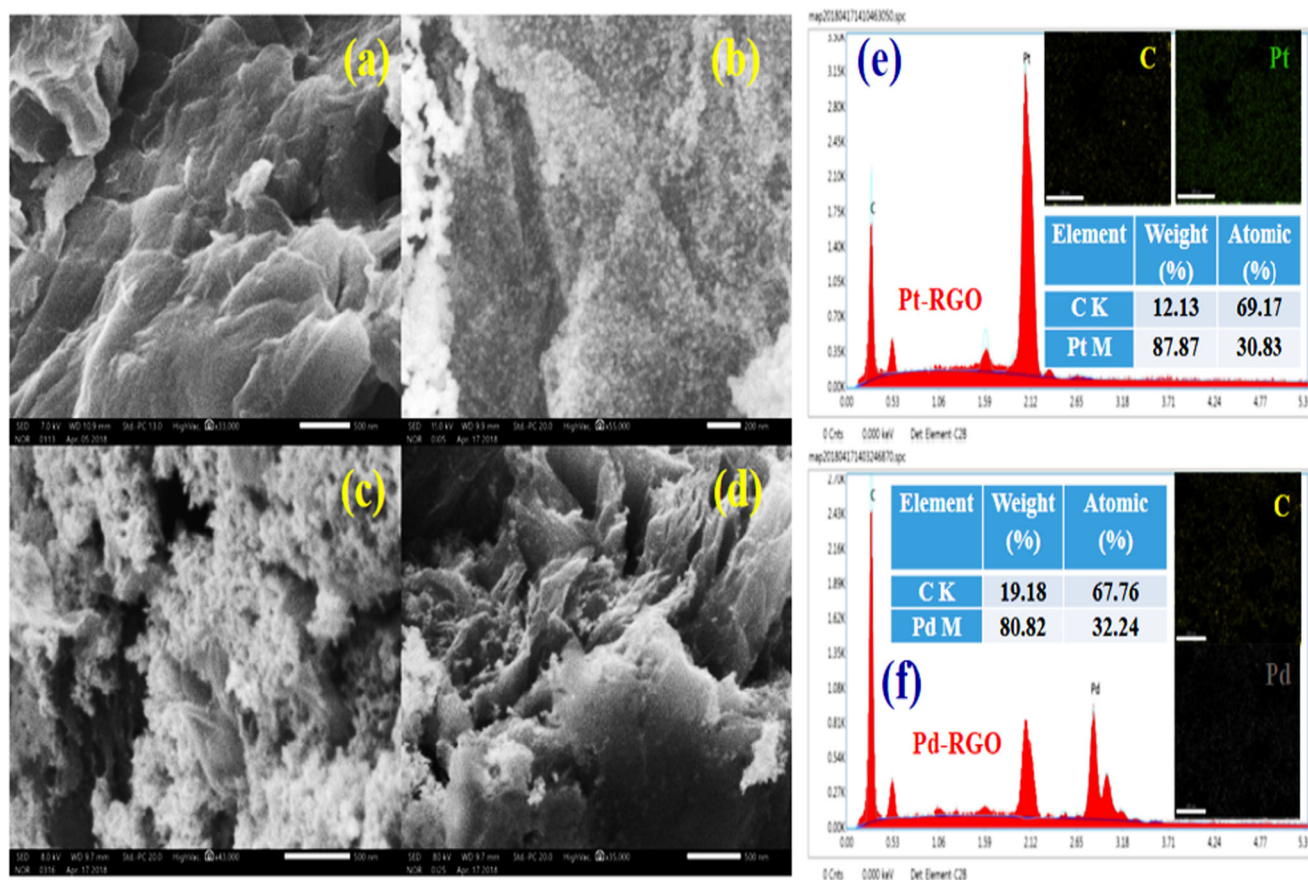


Fig. 5 SEM images of **a** GO, **b** Pt-RGO, **c** Pd-RGO and **d** PtPd-RGO, **e** EDS of Pt-RGO and **f** EDS of Pd-RGO

degree of the disorder and average size of the sp^2 domain for few-layer graphene samples. The I_D/I_G values are found to be 0.74, 0.97, 1.023, 1.018 and 1.029 for GO, RGO, Pt-RGO, Pd-RGO and PtPd-RGO, respectively. Among these all metal-deposited RGO samples have larger I_D/I_G ratio compared with GO concluding the conversion of GO to RGO [39].

FTIR spectroscopy was also used to characterize the reduction of GO. In the IR Spectrum of GO (Fig. 4), the characteristic vibrational modes of O–H ($\sim 3438\text{ cm}^{-1}$) and C=O groups ($\sim 1735\text{ cm}^{-1}$), the deformation peak of O–H groups ($\sim 1383\text{ cm}^{-1}$), the stretching peak of C–OH ($\sim 1260\text{ cm}^{-1}$), and the stretching peak of C–O ($\sim 1020\text{ cm}^{-1}$) are clearly observed, demonstrating that graphite was successfully oxidized to graphene oxide under experimental conditions used. From Fig. 4, it can also be observed that a peak at 2925 cm^{-1} related to C–H stretching vibration along with a peak at 1626 cm^{-1} which can indicated to the vibration of un-oxidized graphite domains. The peak appearance at 1383 cm^{-1} could be attributed to the O–H of carboxylic acid functional group indicating the extent of reduction of graphene oxide into reduced graphene oxide. The FT-IR results of GO and

PtPd-RGO ultra range bimetallic nanospheres well approved with the literature reports [25].

The morphology of the synthesized electrocatalysts was studied by scanning electronic microscopy (Fig. 5). GO possess a sheet like morphology as shown in Fig. 5a. From, Fig. 5b it can be seen that platinum nanoparticles are well distributed on an RGO sheet. Figure 5c indicated that the Pd nanoparticles are well dispersed on an RGO sheet. The non-order PtPd nanospheres are also dispersed on RGO sheets with a little extent of agglomeration as shown in Fig. 5d. The formation of PtPd/RGO ultra-range bimetallic nanospheres can provide a large electrochemically active surface area to facilitate electrochemical reactions at the material's interface while providing respectable stability for yielding high electrocatalytic activity.

Further understanding of the morphology and structure of the as-prepared catalysts was illustrated by HR-TEM (Fig. 6). Figure 6a, b, shows that spherical PtPd nanoparticles are uniformly dispersed on RGO sheet. Majority of the particles possess a metal-on-metal morphology with thicker Pd particles deposited on thinner Pt particles. Figure 6c shows interior lattice with a d-spacing value of 0.22 nm corresponding to PtPd phase. The SAED pattern

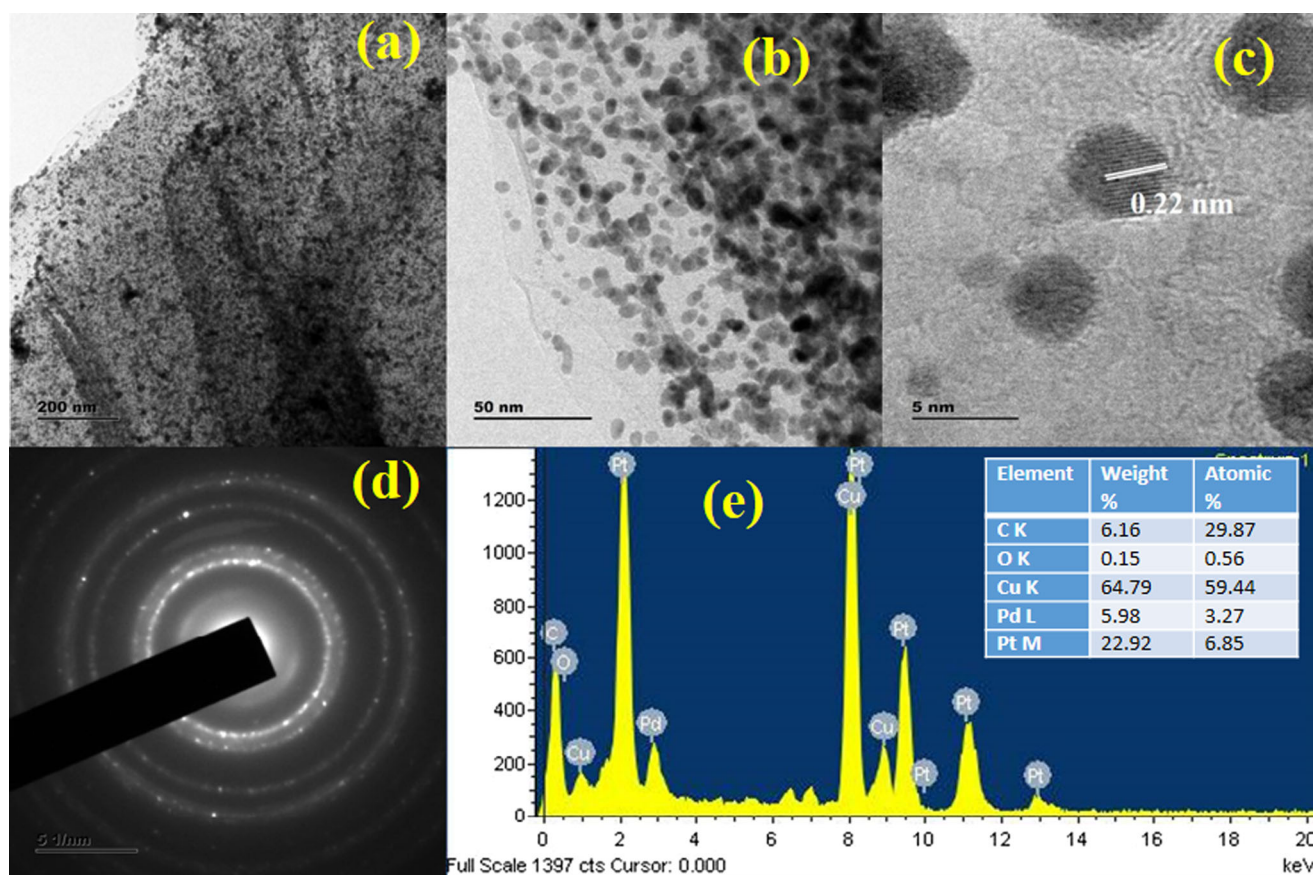


Fig. 6 HR-TEM with EDS images of **a–c** PtPd-RGO, **d** SAED pattern of PtPd-RGO, **e** EDS of PtPd-RGO

shown in Fig. 6d indicates that good crystalline nature of PtPd-RGO catalyst. The EDX pattern shown in Fig. 6e indicates presence of C, O, Cu, Pt and Pd of synthesized PtPd-RGO ultra range bimetallic nanospheres. The appearance of Cu peak is originated from the carbon-coated copper grid used in the analysis and appearance of C and O elements related of RGO. The loading of Pt and Pd is calculated to be 22.92 wt% and 5.98 wt%, respectively on an RGO sheet. The size distribution of PtPd-RGO catalyst range 5–8 nm with an average particle size of 6 nm.

XPS spectra of Pt–Pd-RGO catalyst is shown in Fig. 7. As can be seen from the wide scan survey spectra of XPS (panel a of Fig. 7), the Pt–Pd-RGO catalyst gives the presence of C, O, Pd, and Pt. From the panel (b) of Fig. 7, the C1s XPS spectra exhibited peaks at 284.6 and 289.1 eV related to the C–C and C=O functionalities, respectively of partially reduced graphene oxide. The lowered intensity of C=O peak shows the reduction of GO. O 1s peak is observed at 532.43 eV typical of RGO (panel c of Fig. 7). Further, The Pd 3d XPS spectra (panel d of Fig. 7) exhibit peaks corresponding to the spin-orbital splitting of 3d and gives 3d_{3/2} and 3d_{5/2} peaks at binding energies of 335.42 and 340.38 eV, respectively related to the metallic Pd (0) species indicating the complete reduction of Pd²⁺ to Pd⁰ on

the surface of RGO. In addition, Pt 4f spectra (panel e of Fig. 7) exhibited peaks at 71.36 and 74.67 eV ascribed to the Pt 4f_{7/2} and Pt 4f_{5/2}, respectively related to the metallic Pt (0) species. The XPS results confirms the deposition of Pt and Pd on the RGO surface.

Electrocatalytic Activity Studies of Monometallic and Ultra Range Bimetallic Pt–Pd/RGO NSs

At first, cyclic voltammetry (CV) is utilized to estimate the electrochemical active surface area (ECSA) of Pt-based catalysts. The CV curves of Pt/C, unsupported Pd-RGO, Pt-RGO and PtPd-RGO NSs in H₂SO₄ (0.5 M) are depicted in Fig. 8. The hydrogen absorption/desorption peaks are appeared in between – 0.2 and 0.1 V vs Ag/AgCl (satd. KCl). The oxidation/reduction in between 0.8 to 1.2 V vs Ag/AgCl. The ECSA values are calculated by integrating the charge under hydrogen adsorption/desorption region. For Pt/C, Pd-RGO, Pt-RGO and PtPd-RGO the calculated values of 55.05, 62.3, 78.5 and 83.4 m² g^{–1} respectively are obtained. From the improved ECSA of Pt–Pd/RGO NSs compared to monometallic and commercial Pt/C, a better electrochemical activity can be anticipated. Overall, these results demonstrate that the graphene-supported PtPd ultra-

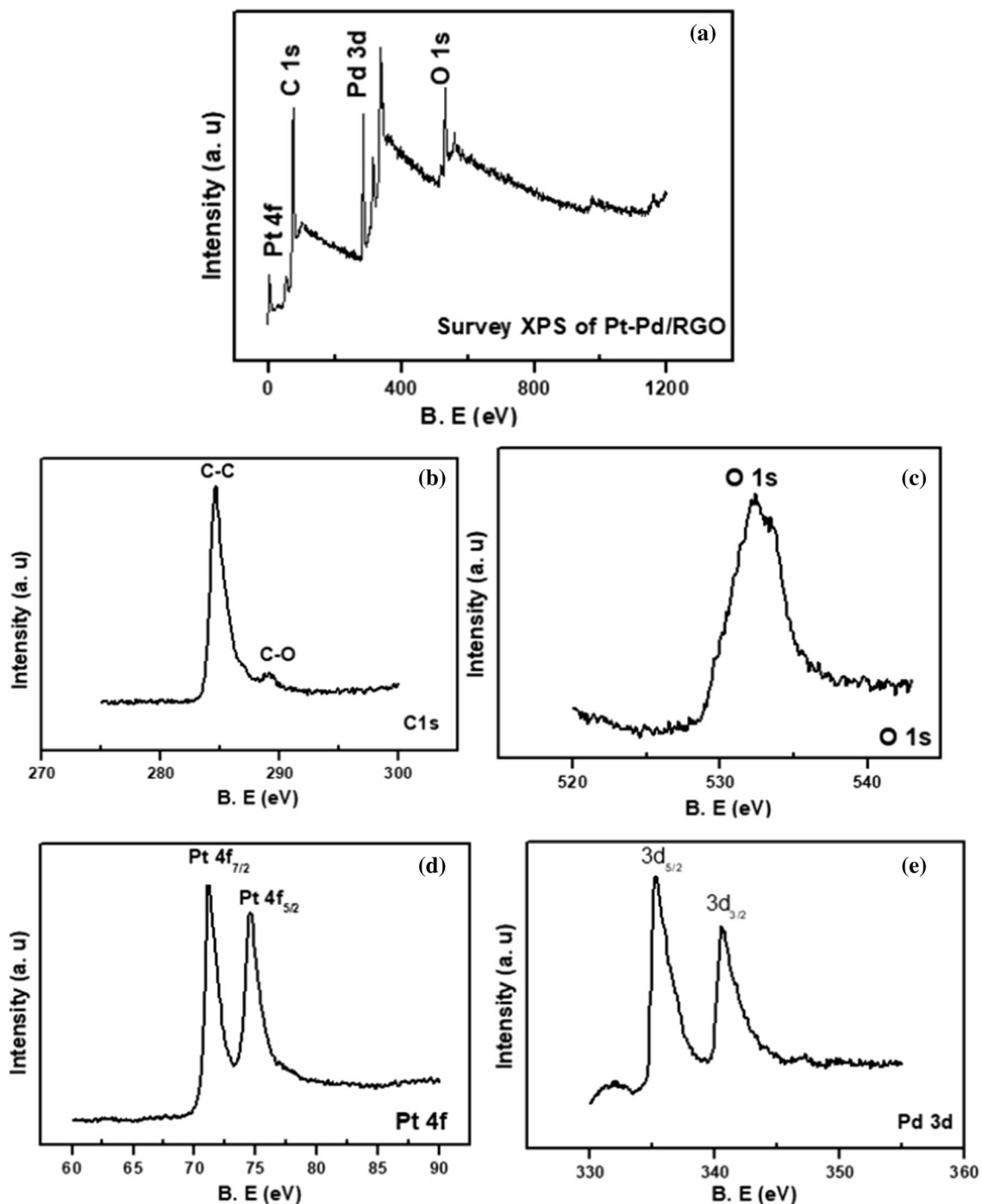


Fig. 7 XPS spectra of Pt–Pd-RGO catalyst. **a** Survey XPS, **b** C1s, **c** O1s, **d** Pt 4f, and **e** Pd 3d spectra

range particles can provide a large surface area for electrocatalysis, which can be attributed to the good distribution of PtPd on the surface of the reduced graphene oxide.

Electrocatalytic oxidation of methanol in acidic solution (0.5 M H₂SO₄) was studied. Figure 9 shows the CV curves of MOR recorded on Pt/C, Pd-RGO, Pt-RGO and PtPd-RGO in 0.5 M H₂SO₄ electrolyte having 1 M CH₃OH solution at a sweep rate of 50 mV s⁻¹ under nitrogen gas

purging. All prepared catalysts exhibit the anodic and cathodic peak in the both forward and reverse scan due to the electro-oxidation of methanol. The peak appeared at around 0.6 V vs Ag/AgCl (satd. KCl) in the forward direction corresponds to the direct oxidation of CH₃OH to CO₂ and another peak around at 0.4 V vs Ag/AgCl (satd. KCl) during the reverse curve is attributed due to the oxidation of carbonaceous intermediates formed in the

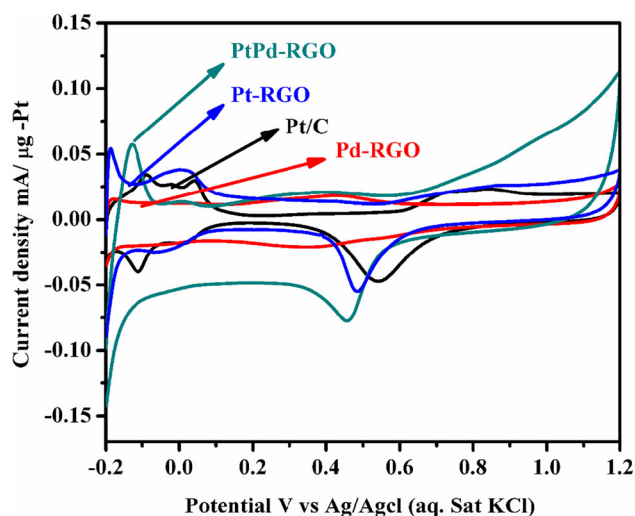


Fig. 8 Cyclic voltammograms (CVs) of PtPd-RGO, Pt-RGO, Pt-C and Pd-RGO catalysts in 0.5 M H₂SO₄ (scan rate at 50 mV s⁻¹)

forward direction. From Fig. 9b the MOR specific activities calculated at 0.6 V vs Ag/AgCl (satd. KCl) (MOR current normalized by ECSA) of Pt/C, Pd-RGO, Pt-RGO and PtPd-RGO are calculated to be 0.198, 0.341, 0.422 and 0.449 mA cm⁻², respectively. 0.51, 0.42, 0.35 and 0.22 mA cm⁻²—ECSA, respectively. Among these catalysts, ultra-range bimetallic electro-catalyst exhibited a better specific activity value compared to the home made monometallic Pt-RGO, Pd-RGO and commercial E-tekPt/C black catalysts. The mass activity (obtained MOR current normalized to the Pt-weight on electrode) is calculated for bimetallic PtPd/RGO NSs as 0.46 mA μg⁻¹-Pt) found to be three-fold higher compared to the commercial E-tek Pt/C black (0.154 mA μg⁻¹-Pt) catalyst. In addition, the specific activities at 0.5 V Vs Ag/AgCl (satd. KCl) where the characteristic CO tolerance of electrocatalyst is important is found to be 0.125, 0.206, 0.250, and 0.170 mA cm⁻², respectively for Pt/C, Pd-RGO, Pt-RGO and PtPd-RGO suggesting the superior CO tolerance ability of RGO-supported catalysts compared to commercial Pt/C [42]. Further, the ratio of forward anodic current density (I_f) and backward cathodic peaks current density (I_b) i.e. I_f/I_b values which gives information on catalyst ability to tolerate CO. The Pt/C, Pd-RGO, Pt-RGO and PtPd/RGO NSs catalysts possess I_f/I_b values of about 0.98, 1.08, 1.20 and 2.12, respectively. PtPd-RGO has greater I_f/I_b values indicating lower amount of accumulated carbonaceous species and improved MOR activity. All electro catalytic results conclusively indicate that ultra-range bimetallic PtPd/RGO NSs have more efficiency towards MOR because of synergetic effect played by platinum and palladium, lower particles size (5–7 nm), well uniform

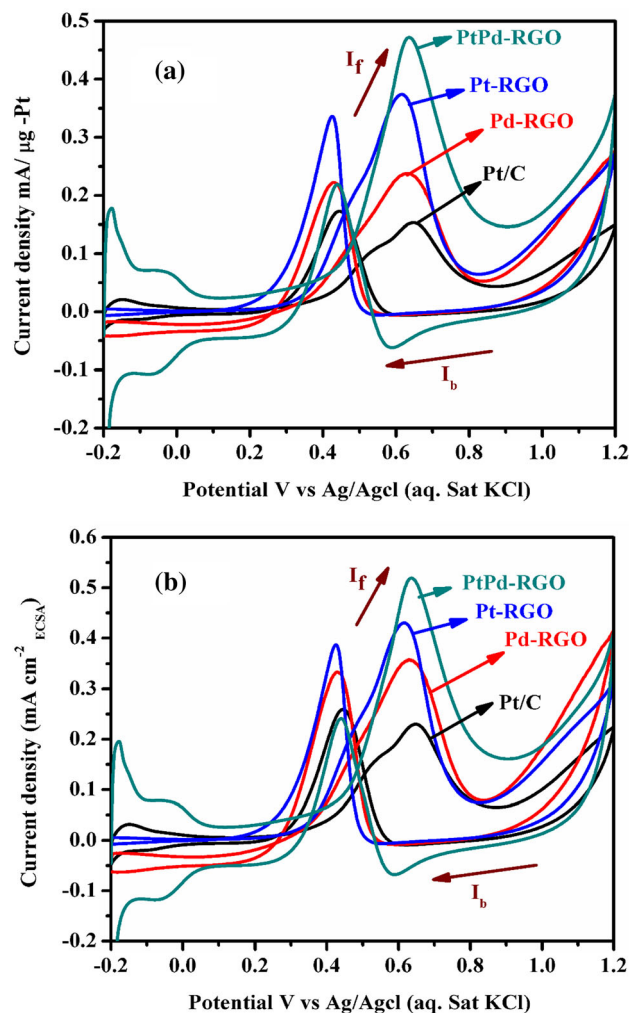


Fig. 9 Cyclic voltammograms (CVs) of PtPd-RGO, Pt-RGO, Pt-C and Pd-RGO catalysts in 0.5 M H₂SO₄ and 1 M CH₃OH (scan rate at 50 mV s⁻¹) **a** Pt mass-normalized current and **b** ECSA-normalized current

deposition on RGO. Furthermore, from literature review it was reported that compared to the conventional carbon supports like carbon black, reduced graphene oxide has more residual oxygen containing groups like epoxide, carboxyl and hydroxyl groups which are capable of promoting oxidation of CO-like species to CO₂ [40–42], also might have contributed to the improved MOR activity.

To assess the durability of the Pt/C, Pd-RGO, Pt-RGO and PtPd/RGO NSs towards MOR, chronoamperometry measurements were performed in 0.5 M H₂SO₄ containing 1 M CH₃OH for a duration of 1000 s under the nitrogen gas purging (Fig. 10). It can be seen that, the initial rapid decline in current density observed for all the catalysts which can be attributed to the accumulation of CO-like intermediates on the active sites of electro-catalysts hindering methanol from further oxidation. Among all the electro catalysts studied, bimetallic PtPd/RGO NSs

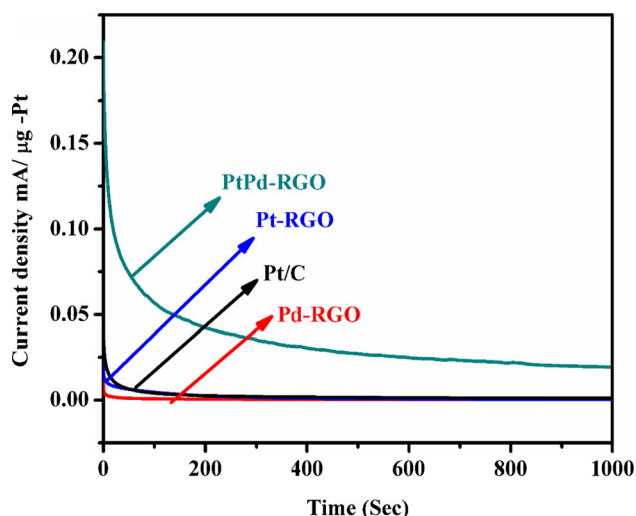


Fig. 10 Current vs time curves of PtPd-RGO, Pt-RGO, Pt/C and Pd-RGO catalysts in 0.5 M H₂SO₄ and 1 M CH₃OH

retained higher current density than the home made mono-metallic catalysts and commercial Pt/C black catalyst during the studied time period indicating its improved durability. Ultra-range particle size confirmed by the HR-TEM observations, uniform distribution of Pt–Pd on the RGO sheets are contributed to more efficient activity and stability for MOR than the commercial Pt/C black, Pd-RGO, Pt-RGO catalysts.

Conclusion

In summary, we have developed a simple hydrothermal approach to prepare ultra-range bimetallic PtPd-RGO electrocatalyst. Uniform PtPd nanospheres arrays were successfully grown on RGO nanosheet surfaces. Most importantly, the bimetallic PtPd-RGO nanospheres exhibited a higher catalytic activity and stability toward the methanol oxidation reaction (MOR) with a mass activity of 0.46 mA μg⁻¹-Pt and an I_p/I_b ratio of 2.12 were achieved, respectively. This new and convenient approach demonstrated can be extended to prepare other related electrocatalysts for possible enhancement of MOR to improve the performance for DMFCs. The composite structure combining graphene-based nanostructure and Pt-based nanospheres may also be useful in other electrochemical applications.

Acknowledgements This research was financially supported by a university grants commission (UGC), New Delhi under the Award No. 2-362/2013 (SR). We also acknowledge instrumental support University of Hyderabad, Hyderabad is gratefully acknowledged.

References

- Z. Ruizhong and C. Wei (2013). *J. Mater. Chem. A* **1**, 11457–11464.
- X. Zhao, J. Zhang, L. Wang, H. X. Li, Z. Liu, and W. Chen (2015). *ACS Appl. Mater. Interfaces*. **7**, 26333–26339.
- W. Hong, C. Shang, J. Wang, and E. Wang (2015). *Energy Environ. Sci.* **8**, 2910–2915.
- X. Du, S. Luo, H. Du, M. Tang, X. Huang, and P. K. Shen (2016). *J. Mater. Chem. A* **4**, 1579–1585.
- P. Pattanayak, N. Pramanik, P. Kumar, and P. P. Kundu (2017). *Int. J. Hydrogen Energy* **43**, 11505–11519.
- Y. Lu, Y. Jiang, H. Wu, and W. Chen (2013). *J. Phys. Chem. C* **117**, 2926–2938.
- H. S. Liu and J. J. Zhang *Electrocatalysis of direct methanol fuel cells: from fundamentals to applications* (Wiley-VCH Verlag GmbH & Co., KGaA, Weinheim, 2009).
- H. Yin, H. Tang, D. Wang, Y. Gao, and Z. Tang (2012). *ACS Nano* **6**, 8288–8297.
- S. Zhao, H. Yin, L. Du, G. Yin, Z. Tang, and S. Liu (2014). *J. Mater. Chem. A* **2**, 3719–3724.
- S. Zhao, Y. Li, H. Yin, Z. Liu, E. Luan, F. Zhao, Z. Tang, and S. Liu (2015). *Sci. Adv.* **1**, 1–9.
- S. Zhao, Y. Wang, J. Dong, C. T. He, H. Yin, P. An, K. Zhao, X. Zhang, C. Gao, L. Zhang, J. Lv, J. Wang, J. Zhang, A. M. Khattak, N. A. Khan, Z. Wei, J. Zhang, S. Liu, H. Zhao, and Z. Tang (2016). *Nat. Energy* **1**, 1–10.
- Y. Li, L. Tang, and J. Li (2009). *Electrochem Commun.* **11**, 846–849.
- P. Santhosh, A. Gopalan, and K. P. Lee (2006). *J. Catal.* **238**, 177–185.
- Y. Zhao, Z. Lu, J. Tian, S. Nie, and N. Zhen (2011). *Electrochim. Acta* **56**, 1967–1972.
- Y. Qu, C. Li, L. Wang, Y. Gao, J. Rao, and G. Yin (2016). *Int. J. Hydrogen Energy* **41**, 14036–14046.
- M. S. Ekrami-Kakhki, N. Farzaneh, and E. Fathi (2017). *Int. J. Hydrogen Energy* **42**, 21131–21145.
- G. Chang, Z. Cai, H. Jia, Z. Zhang, X. Liu, Z. Liu, R. Zhu, and Y. He (2018). *Int. J. Hydrogen Energy* **43**, 12803–12810.
- L. Zhang, L.-X. Ding, H. Chen, D. Li, S. Wang, and H. Wang (2017). *Small* **13**, 1604000.
- X. W. Xie, J. J. Lv, L. Liu, A. J. Wang, J. J. Feng, and Q. Q. Xu (2017). *Int. J. Hydrogen Energy* **42**, 2104–2115.
- A. B. Yousaf, M. Imran, A. Zeb, T. Wen, X. Xie, Y. F. Jiang, C. Z. Yuan, and A. W. Xu (2016). *Electrochimica Acta* **197**, 117–125.
- C. H. Fang, J. Zhao, G. L. Zhao, L. Kuai, and B. Y. Geng (2016). *Nanoscale* **8**, 14971–14978.
- S. L. Lu, K. Eid, D. H. Ge, J. Guo, L. Wang, H. J. Wang, and H. Gu (2017). *Nanoscale* **9**, 1033–1039.
- Y. M. Hu, A. M. Zhu, Q. G. Zhang, and Q. L. Liu (2016). *Int. J. Hydrogen Energy* **41**, 11359–11368.
- Q. Q. Lu, H. J. Wang, K. Eid, Z. A. Allothman, V. Malgras, Y. Yamauchi, and L. Wang (2016). *Chem. Asian J.* **11**, 1939–1944.
- E. Sunanda, P. Venkata Ramana, Z. Hong, G. Sreenivasa Kumar, N. Rammanohar Reddy, and S. Adinarayana Reddy (2018). *Int. J. Hydrogen Energy* **43**, 4115–4124.
- Y. Liu, M. Chi, V. Mazumder, K. L. More, S. Soled, J. D. Henao, and S. Sun (2011). *Chem. Mater.* **23**, 4199–4203.
- T. Y. Yung, T. Y. Liu, K. S. Wang, C. C. Liu, S. H. Wang, P. T. Chen, and C. Y. Chao (2016). *Catalysts* **6**, 1–11.
- Y. J. Wang, J. B. Zang, L. Dong, H. Pan, Y. G. Yuan, and Y. H. Wang (2013). *Electrochim. Acta* **113**, 583–590.
- Z. Hui, X. Xu, P. Gu, C. Li, P. Wu, and C. Cai (2011). *Electrochim. Acta* **56**, 7064–7070.

30. H. Zhang, M. Jin, and Y. Xia (2012). *Chem. Soc. Rev.* **41**, 8035–8049.
31. F. Ren, H. Wang, C. Zhai, M. Zhu, R. Yue, Y. Du, P. Yang, J. Xu, and W. Lu (2014). *ACS Appl. Mater. Interfaces.* **6**, 3607–3614.
32. D. B. Huang, Q. Yuan, H. H. Wang, and Z. Y. Zhou (2014). *Chem. Commun.* **50**, 13551–13554.
33. A. K. Geim and K. S. Novoselov (2007). *Nat. Mater.* **6**, 183–191.
34. M. Liu, R. Zhang, and W. Chen (2014). *Chem. Rev.* **114**, (2014), 5117–5160.
35. T. D. Thanh, J. Balamurugan, S. H. Lee, N. H. Kim, and J. H. Lee (2016). *Biosens. Bioelectron.* **81**, 259–267.
36. J. Samdani, K. Samdani, N. H. Kim, and J. H. Lee (2017). *Appl. Surf. Sci.* **399**, 95–105.
37. P. Hung, K. Lau, B. Fox, N. Hameed, J. H. Lee, and D. Hui (2018). *Compos. B* **133**, 240–257.
38. J. H. Lee, J. S. Lee, T. Kuila, N. H. Kim, and D. Jung (2013). *Compos. B* **51**, 98–105.
39. P. Qiu, J. Bi, X. Zhang, and S. Yang (2007). *ACS Sustain. Chem. Eng.* **5**, 4205–4213.
40. J. Chen, M. Wang, B. Liu, Z. Fan, K. Cui, and Y. Kuang (2006). *J. Phys. Chem. B* **110**, 11775–11779.
41. J. N. Zheng, J. J. Lv, S. S. Li, M. W. Xue, A. J. Wang, and J. J. Feng (2014). *J. Mater. Chem. A* **2**, 3445–3451.
42. J. Suntivich, Z. Xu, C. E. Carlton, J. Kim, B. Han, S. W. Lee, N. Marzari, L. F. Allard, H. A. Gasteiger, K. H. Schifferli, and Y. S. Horn (2013). *J. Am. Chem. Soc.* **135**, 7985–7991.

Publisher's Note Springer Nature remains neutral with regard to jurisdictional claims in published maps and institutional affiliations.